MOX-Report No. 66/2026

A stability-preserving polytopal discontinuous Galerkin method for the Fisher-Kolmogorov model with applications to neurodegenerative diseases

Antonietti, P.F.;Bonizzoni, F.;Corti, M.; De March, N.;Di Noto, S.;Regazzoni, F.

MOX, Dipartimento di Matematica
Politecnico di Milano, Via Bonardi 9 - 20133 Milano (Italy)

mox-dmat@polimi.it https://mox.polimi.it

A stability-preserving polytopal discontinuous Galerkin method for the Fisher-Kolmogorov model with applications to neurodegenerative diseases*

Paola F. Antonietti [1], Francesca Bonizzoni [1], Mattia Corti [1], Nicola De March [1], Salvatore Di Noto[1], and Francesco Regazzoni [1]

[1] *MOX - Modeling and Scientific Computing Laboratory, Dipartimento di Matematica, Politecnico di Milano, Piazza Leonardo da Vinci 32, Milan, 20133, Italy*

Abstract

The Fisher–Kolmogorov model is one of the most widely used models in the study of neurodegenerative diseases, owing to its simple structure as a nonlinear reaction–diffusion equation. In particular, it is commonly employed to describe proteinopathies such as Alzheimer's and Parkinson's diseases. Under suitable assumptions, non-negativity of the solution is guaranteed at the continuous level, which is physically relevant since the solution represents a relative concentration. However, this property is not generally preserved at the discrete level, potentially leading to unphysical and unstable numerical approximations. In this work, we analyze a modified version of the Fisher–Kolmogorov model that stabilizes the dynamics around the unstable equilibrium $c = 0$. For the spatial discretization, we adopt a discontinuous Galerkin method on polygonal and polyhedral meshes, coupled with the Crank–Nicolson scheme for time integration. We derive stability and *a-priori* error estimates for the semi-discrete problem. The theoretical findings are supported by numerical experiments, including convergence studies in both two and three dimensions. Finally, we validate the model through simulations of α-synuclein diffusion in a two-dimensional agglomerated brain section, demonstrating the high-order accuracy and robustness of the proposed method.

1 Introduction

Neurodegenerative diseases comprise a class of disorders that impair neuronal function. Among them, proteinopathies such as Alzheimer's and Parkinson's diseases are the most prevalent and have been extensively studied. These pathologies are characterized by the misfolding and aggregation of prion-like proteins into toxic, insoluble conformations [1]. For instance, α-synuclein [2] and amyloid-β [3, 4] undergo such processes in Parkinson's and Alzheimer's diseases, respectively.

Understanding and predicting the evolution of these processes is crucial for improving diagnosis and patient care. In recent years, several mathematical models describing *prion-like* dynamics have been proposed. In particular, models based on the Smoluchowski equation have been extensively studied [5, 6].

*__Fundings__: This work is partially funded by the European Union (ERC SyG, NEMESIS, project number 101115663). Views and opinions expressed are, however, those of the authors only and do not necessarily reflect those of the European Union or the European Research Council Executive Agency. Neither the European Union nor the granting authority can be held responsible for them. The present research is part of the activities of the Dipartimento di Eccellenza 2023-2027 grant, funded by MUR. PFA, FB, MC, NDM, and FR are members of INdAM-GNCS.

Due to their complexity, simplified formulations have been introduced, leading to nonlinear reaction–diffusion models such as the heterodimer model and the Fisher–Kolmogorov (FK) equation [7, 8].

Alongside the development of new theoretical models, a variety of numerical methods have been proposed to approximate their solutions. For the FK model, several approaches have been explored, including finite element methods [7, 9, 10], finite difference schemes [11], boundary element methods [12], and discontinuous Galerkin (DG) methods [13]. Since the FK model aims to study the diffusion of misfolded proteins in the brain, it is important that the solution is non-negative from a physical point of view. Under suitable hypotheses, this property is guaranteed at the continuous level. At the numerical one, instead, it is not automatically inherited; thus, structure-preserving formulations based on the DG methods have been proposed to solve the issue [14, 15].

In this work, we propose and analyze a numerical method based on a stabilized version of the FK model (SFK). The modification concerns the nonlinear reaction term, for which an absolute-value stabilization is introduced. This preserves the original structure of the equation while avoiding the issues related to strong nonlinearities in interior penalty discretizations (see [14]). A key property is that the proposed SFK model is strongly consistent with the original FK equation for positive solutions, which are typical in applications [16]. To approximate the solution, we employ a high-order discontinuous Galerkin method on general polygonal and polyhedral meshes (PolyDG) for the spatial discretization, coupled with a second-order implicit time integration scheme such as Crank–Nicolson. This choice ensures high-order accuracy and enables the treatment of complex geometries, providing significant flexibility in mesh generation, particularly for brain domains.

Through a rigorous theoretical analysis, we establish improved stability and convergence properties of the proposed method compared to the original formulation in [13], in both two and three dimensions. Moreover, the structure of the method naturally extends the analysis to general polytopal meshes [17, 18], which is particularly relevant for brain applications employing mesh agglomeration strategies [19].

Finally, we present numerical experiments that validate the theoretical findings, including optimal convergence rates and solution accuracy. We also apply the model to a full brain section, showing that the resulting diffusion patterns of misfolded proteins are consistent with observations reported in the medical literature [20, 21]. A comparison between the SFK and standard FK models further demonstrates that the former provides reliable results even at lower polynomial degrees, making it a robust and efficient computational approach.

The thesis is organized as follows. In Section 2, we recall the FK model and its functional setting. In Section 3, we present some preliminary technical backgrounds and the PolyDG space discretization of the problem and we introduce the SFK model and its formulation. In Section 4, we prove the stability of the SFK model. In Section 5, we derive an *a-priori* error estimate of the semi-discretized problem. In Section 6, we introduce the Crank-Nicolson time discretization scheme for the SFK model. In Sections 7 and 8 we report the numerical results, starting from some convergence tests in the case of a given manufactured solution and the simulations of the diffusion of α-synuclein protein in Parkinson's disease in a two-dimensional brain section reconstructed from medical images, respectively. Finally, in Section 9, we draw some conclusions and discuss possible future developments.

2 The Fisher-Kolmogorov model

In this section, we present the FK model, used to describe the reaction and diffusion of interacting species [7]. We consider the domain $\Omega \subset \mathbb{R}^d$ with $d = 2, 3$ and the time interval $(0, T)$, being $T > 0$ a fixed final time. We denote by $c = c(\boldsymbol{x}, t)$ the relative concentration of misfolded proteins over the theoretical maximum that can be derived as in [7] under the assumption of constant baseline concentration of healthy state protein. The variable c has to be in the range $[0, 1]$, where 0 stands for the absence of misfolded proteins and 1 for total presence of them. The strong formulation of the FK model reads:

$$
\begin{aligned}
\frac{\partial c}{\partial t} &= \nabla \cdot (\mathbf{D}\nabla c) + \alpha c(1-c) + f \qquad && \text{in } \Omega \times (0,T], \\
(\mathbf{D}\nabla c) \cdot \boldsymbol{n} &= \phi_N && \text{on } \Gamma_N \times (0,T], \\
c &= c_D && \text{on } \Gamma_D \times (0,T], \\
c(\cdot,0) &= c_0 && \text{in } \Omega.
\end{aligned} \tag{1}
$$

In Equation (1), the reaction parameter $\alpha \geq 0$ represents the local conversion rate of healthy proteins into misfolded ones. The diffusion tensor $\mathbf{D} = \mathbf{D}(\boldsymbol{x})$ describes the spreading of misfolded proteins inside the domain and is obtained as the combination of an axonal diffusion of magnitude $d_{axn} \geq 0$ and an extracellular diffusion effect of magnitude $d_{ext} \geq 0$, such that:

$$
\mathbf{D}(\boldsymbol{x}) = d_{ext}\mathbf{I} + d_{axn}\boldsymbol{a}(\boldsymbol{x}) \otimes \boldsymbol{a}(\boldsymbol{x}), \tag{2}
$$

where $\boldsymbol{a}(\boldsymbol{x})$ is the axonal fibres orientation at point $\boldsymbol{x} \in \Omega$. The axonal direction is the main orientation of the connections between the neurons (axons), which can be derived from Diffusion Weighted Imaging (DWI) [7]. The forcing term $f = f(\boldsymbol{x}, t)$ models the external addition/removal of mass. The Neumann condition prescribes a sufficiently regular flux $\phi_N = \phi_N(\boldsymbol{x}, t)$ on the boundary of the domain denoted by Γ_N, while the Dirichlet condition imposes a concentration value $c_D = c_D(\boldsymbol{x}, t)$ on the boundary portion Γ_D. We note that $\Gamma_N \cup \Gamma_D = \partial\Omega$ and $\Gamma_N \cap \Gamma_D = \emptyset$.

We define the Sobolev spaces as follows $W_D = \left\{w \in H^1(\Omega) : w|_{\Gamma_D} = c_D\right\}$ and $W_0 = H^1_{\Gamma_D}(\Omega)$. When $|\Gamma_D| = 0$ and $\Gamma_N = \partial\Omega$, we say that $W_D = W_0 = H^1(\Omega)$. We employ a standard definition of the scalar product in $L^2(\Omega)$, represented by $(\cdot,\cdot)_\Omega$, and of its induced norm $\|\cdot\|$, whose definition can be extended component-wise to vector-valued and tensor-valued functions [16]. Then we can introduce the following assumption on coefficients' regularity.

Assumption 2.1 (Coefficients' regularity)**.** We assume the following regularities for the coefficients and the forcing terms appearing in Equation (1):

- $\mathbf{D} \in L^\infty(\Omega, \mathbb{R}^{d\times d})$ and $\exists d_0 > 0$ such that: $d_0|\boldsymbol{\psi}|^2 \leq \boldsymbol{\psi}^T\mathbf{D}\boldsymbol{\psi} \quad \forall \boldsymbol{\psi} \in \mathbb{R}^d$.
- $f \in L^2((0,T]; L^2(\Omega))$.
- $\phi_N \in L^2((0,T]; L^2(\Gamma_N))$.
- $c_D \in L^2((0,T]; H^{1/2}(\Gamma_D))$.
- $c_0 \in L^2(\Omega)$.

The last step to derive the weak formulation of problem is to introduce:

$$
a(c,w) = (\sqrt{\mathbf{D}}\nabla c, \sqrt{\mathbf{D}}\nabla w)_\Omega \qquad \forall c \in W_D, \forall w \in W_0, \tag{3}
$$

$$
F(w) = (f,w)_\Omega + (\phi_N, w)_{\Gamma_N} \qquad \forall w \in W_0. \tag{4}
$$

Then, the weak formulation of problem (1) reads: Find $c = c(t) \in W_D$ such that for any $t \in (0,T]$:

$$
\begin{aligned}
\left(\frac{\partial c}{\partial t}, w\right)_\Omega + a(c,w) - (\alpha c, w)_\Omega + \left(\alpha c^2, w\right)_\Omega &= F(w) \qquad && \forall w \in W_0, \\
c(\cdot,0) &= c_0 && \text{in } \Omega.
\end{aligned} \tag{5}
$$

Remark 2.1. *Under Assumption 2.1, if* $f = 0$, $\phi_N = 0$ *and* $\Gamma_D = \emptyset$ *with* $c_0(\boldsymbol{x}) \in [0,1]$ $\forall \boldsymbol{x} \in \Omega$, $c_0(\boldsymbol{x})$ *not identically equal to zero, it can be proved that the FK equation admits a traveling wave solution. Moreover,*

we can state that the solution $c(\boldsymbol{x},t) \in [0,1]\ \forall \boldsymbol{x} \in \Omega,\ t > 0$. *This translates into the existence of two equilibrium points: an unstable equilibrium at* $c = 0$ *and a stable one at* $c = 1$*, such that:*

$$\lim_{t \to +\infty} c(\boldsymbol{x},t) = 1.$$

3 Polygonal discontinuous Galerkin semi-discrete formulation

In this section, we construct a space approximation for problem (5) using the PolyDG method [13]. First, we introduce a mesh partition $\mathscr{T}_h$ of the domain Ω made of disjoint polygonal/polyhedral elements K. For each of them, we define its measure $|K|$ and its diameter h_K such that $h = \max_{K \in \mathscr{T}_h}\{h_K\} < 1$. From now on, we will use the following notation $x \lesssim y$ to say that $\exists C > 0 : x \leq Cy$, where the constant C depends on the model parameters and on the polynomial degree p but is independent on the mesh size h. The interface is the intersection of the $(d-1)$-dimensional facets of two neighbouring elements:

- for $d = 2$, the interfaces are line segments and a set of segments is denoted with $\mathscr{F}_h$;
- for $d = 3$, any interface is a generic polygon and we assume that each of them can be decomposed into planar triangles, whose set is denoted with $\mathscr{F}_h$.

The set $\mathscr{F}_h$ can be seen as the union of interior faces ($\mathscr{F}_h^I$) and exterior faces ($\mathscr{F}_h^B$) lying on the domain boundary $\partial\Omega$. The boundary faces can be split taking into account the type of boundary condition: $\mathscr{F}_h^B = \mathscr{F}_h^D \cup \mathscr{F}_h^N$, where $\mathscr{F}_h^D$ and $\mathscr{F}_h^N$ are the boundary faces contained in Γ_D and Γ_N, respectively.

In this work we introduce two different mesh regularity assumptions that will be exploited in different part of the theory developed in the next sections.

Assumption 3.1 (Shape-regular mesh [22])**.** The mesh sequence $\{\mathscr{T}_h\}_h$ satisfies the following properties:

1. **Shape regularity**: $c_1 h_K^d \ \leq\ q|K| \leq\ c_2 h_K^d, \quad \forall K \in \mathscr{T}_h$.
2. **Contact regularity**: $\forall F \in \mathscr{F}_h$ with $F \subseteq \overline{K}$ for some $K \in \mathscr{T}_h$, it holds $h_K^{d-1} \lesssim |F|$, where $|F|$ is the Hausdorff measure of the face F.
3. **Submesh condition**: there exists a shape-regular, conforming, matching simplicial submesh $\widetilde{\mathscr{T}_h}$ such that:
   - $\forall \widetilde{K} \in \widetilde{\mathscr{T}_h} \quad \exists K \in \mathscr{T}_h$: $\widetilde{K} \subseteq K$.
   - The family $\{\widetilde{\mathscr{T}_h}\}_h$ is shape and contact regular.
   - $\forall \widetilde{K} \in \widetilde{\mathscr{T}_h},\ K \in \mathscr{T}_h$ with $\widetilde{K} \subseteq K$, it holds $h_K \lesssim h_{\widetilde{K}}$.

Assumption 3.2 (Polytopic-regular mesh [18])**.** The mesh sequence $\{\mathscr{T}_h\}_h$ satisfies the following properties:

1. **Polytopic-regularity**: let $\{S_K^F\}_{F \subset \partial K}$ be a set of non-overlapping d-dimensional simplices contained in K, then:

$$\forall K \in \mathscr{T}_h \quad \exists \{S_K^F\}_{F \subset \partial K} \text{ such that } \quad \forall F \subset \partial K \quad \overline{F} = \partial\overline{K} \cap \overline{S_K^F} \text{ and } h_K \lesssim d|S_K^F|\ |F|^{-1}.$$

2. **Covering mesh condition**: For each $\mathscr{T}_h \in \{\mathscr{T}_h\}_h$ there exists a shape-regular, simplicial covering $\hat{\mathscr{T}}_h$ such that for each pair $K \in \mathscr{T}_h$ and $\hat{K} \in \hat{\mathscr{T}}_h$ with $\hat{K} \subset K$ it holds $h_K \lesssim h_{\hat{K}}$ and $\max_{K \in \mathscr{T}_h}\{|K'|\} \lesssim 1$ where $K' \in \mathscr{T}_h : K' \cap \hat{K} \neq 0, \hat{K} \in \hat{\mathscr{T}}_h, K \subset \hat{K}$.
3. **Local bounded variation property**: $\forall F \in \mathscr{F}_h F \subset \partial K_1 \cap \partial K_2 \quad K_1, K_2 \in \mathscr{T}_h \Rightarrow h_{K_1} \lesssim h_{K_2} \lesssim h_{K_1}$ where the hidden constants are independent of the number of faces of K_1 and K_2.

Remark 3.1. We remark that Assumption 3.1 is more restrictive than 3.2, which requires milder hypothesis on the size of the element faces. ∎

We define $\mathbb{P}_p(K)$ to be the space of polynomials of total degree $p \geq 1$ over a mesh element K. Then, we introduce the following discontinuous finite element space $W_h^{\mathrm{DG}} = \left\{ w \in L^2(\Omega) : w|_K \in \mathbb{P}_p(K) \ \ \forall K \in \mathscr{T}_h \right\}$. Let $F \in \mathscr{F}_h$ be a face shared by the elements $K^{\pm}$, then $\boldsymbol{n}^{\pm}$ is the corresponding unit normal vector on face F pointing exterior to $K^{\pm}$. For sufficiently regular scalar-valued functions v and vector-valued functions $\boldsymbol{q}$, we define the following trace operators [23], respectively:

- jump operator $[\![\cdot]\!]$ on $F \in \mathscr{F}_h^I$: $[\![v]\!] = v^+\boldsymbol{n}^+ + v^-\boldsymbol{n}^-, \quad [\![\boldsymbol{q}]\!] = \boldsymbol{q}^+ \cdot \boldsymbol{n}^+ + \boldsymbol{q}^- \cdot \boldsymbol{n}^-$;
- average operator $\{\!\{\cdot\}\!\}$ on $F \in \mathscr{F}_h^I$: $\{\!\{v\}\!\} = \frac{1}{2}(v^+ + v^-), \quad \{\!\{\boldsymbol{q}\}\!\} = \frac{1}{2}(\boldsymbol{q}^+ + \boldsymbol{q}^-)$,

where the superscripts $\pm$ refer to the traces of the functions on F taken within the interior to $K^{\pm}$ respectively. Moreover, we can introduce similar operators on the face $F \in \mathscr{F}_h^D$ associated with the cell $K \in \mathscr{T}_h$ with $\boldsymbol{n}$ outward unit normal on $\partial\Omega$:

- jump operator $[\![\cdot]\!]$ on $F \in \mathscr{F}_h^D$: $[\![v]\!] = (v - g)\boldsymbol{n}, \quad [\![\boldsymbol{q}]\!] = (\boldsymbol{q} - \boldsymbol{g}) \cdot \boldsymbol{n}$;
- average operator $\{\!\{\cdot\}\!\}$ on $F \in \mathscr{F}_h^D$: $\{\!\{v\}\!\} = v, \quad \{\!\{\boldsymbol{q}\}\!\} = \boldsymbol{q}$,

where g and $\boldsymbol{g}$ are the corresponding Dirichlet boundary conditions. Additionally, we introduce the following broken Sobolev spaces $H^r(\mathscr{T}_h) = \left\{ w_h \in L^2(\Omega) : w_h|_K \in H^r(K) \ \forall K \in \mathscr{T}_h \right\}$ for $r \geq 1$ and the shorthand notation for the L^2-norm on a set of faces $\mathscr{F}$ as $||\cdot||_{\mathscr{F}}^2 = \sum_{F \in \mathscr{F}} ||\cdot||_{L^2(F)}^2$.

3.1 Interior-penalty DG semi-discrete formulation

Before presenting the semi-discrete formulation, we need to define the penalization function $\eta : \mathscr{F}_h \to \mathbb{R}^+$:

$$\eta = \eta_0 \begin{cases} \dfrac{p^2}{\{h\}_{\mathrm{H}}} & \text{on } F \in \mathscr{F}_h^I, \\ \dfrac{p^2}{h} & \text{on } F \in \mathscr{F}_h^D, \end{cases} \tag{6}$$

where the operator $\{\cdot\}_{\mathrm{H}}$ stands for the harmonic average on $F \in \mathscr{F}_h^I$ and η_0 is a suitable parameter, which has to be large enough to achieve stability. We define the bilinear form $\mathscr{A} : W_h^{\mathrm{DG}} \times W_h^{\mathrm{DG}} \to \mathbb{R}$ as:

$$\mathscr{A}(c, w) = \int_\Omega \nabla_h c \cdot \nabla_h w + \int_{\mathscr{F}_h^I \cup \mathscr{F}_h^D} \Big(\eta [\![c]\!] \cdot [\![w]\!] - \{\!\{\mathbf{D}\nabla c\}\!\} \cdot [\![w]\!] - [\![c]\!] \cdot \{\!\{\mathbf{D}\nabla w\}\!\} \Big) d\sigma \quad \forall c, w \in W_h^{\mathrm{DG}}, \tag{7}$$

where $\nabla_h \cdot$ is the elementwise gradient [23].

Then, the semi-discrete PolyDG formulation reads: Find $c_h(t) \in W_h^{\mathrm{DG}}$ such that $\forall t > 0$:

$$\begin{aligned} \left(\frac{\partial c_h(t)}{\partial t}, w_h \right)_\Omega + \mathscr{A}(c_h(t), w_h) - (\alpha c_h(t), w_h)_\Omega + (\alpha c_h^2(t), w_h)_\Omega &= F(w_h) \qquad \forall w_h \in W_h^{\mathrm{DG}}, \\ c_h(0) &= c_h^0 \qquad \text{in } \Omega_h, \end{aligned} \tag{8}$$

where $c_h^0 \in W_h^{\mathrm{DG}}$ is a suitable approximation of c_0. For the analysis of the method in (8), we refer to [13].

3.2 The stabilized FK model

In this section, we propose a stabilized version of the FK model (SFK) based on a new definition of the reaction term. The strong formulation of the SFK model reads:

$$\begin{aligned} \frac{\partial \hat{c}}{\partial t} &= \nabla \cdot (\mathbf{D}\nabla \hat{c}) + \alpha|\hat{c}|(1-\hat{c}) + f && \text{in } \Omega \times (0,T], \\ (\mathbf{D}\nabla \hat{c}) \cdot \boldsymbol{n} &= \phi_N && \text{on } \Gamma_N \times (0,T], \\ \hat{c} &= c_D && \text{on } \Gamma_D \times (0,T], \\ \hat{c}(\cdot,0) &= c_0 && \text{in } \Omega. \end{aligned} \tag{9}$$

In Equation (9), we recover the same coefficients of Equation (1) and Assumption 2.1 still holds for the SFK model.

Remark 3.2. The choice of $|\hat{c}|$ in the reaction term transforms the unstable equilibrium $c = 0$ into a stable one, avoiding the solution from diverging when it is negative. At the discrete level, the same property is preserved providing a stabilization or the original method (8). Moreover, the solutions of the classical FK model and of the SFK model coincide at the continuous level when $c(\boldsymbol{x}, t) \geq 0$ and $\hat{c}(\boldsymbol{x}, t) \geq 0$, respectively, such that strong consistency is guaranteed among the two. ∎

The resulting semi-discrete PolyDG formulation of the SFK equation reads: Find $\hat{c}_h(t) \in W_h^{\mathrm{DG}}$ such that $\forall t > 0$:

$$\begin{aligned} \left(\frac{\partial \hat{c}_h(t)}{\partial t}, w_h\right)_\Omega + \mathscr{A}(\hat{c}_h(t), w_h) - (\alpha|\hat{c}_h|(t), w_h)_\Omega + (\alpha|\hat{c}_h(t)|\hat{c}_h(t), w_h)_\Omega &= F(w_h) && \forall w_h \in W_h^{\mathrm{DG}}, \\ \hat{c}_h(0) &= c_h^0 && \text{in } \Omega_h. \end{aligned} \tag{10}$$

3.3 Preliminary estimates and properties

First of all let us introduce the two following DG-norm:

$$\|v\|_{\mathrm{DG}}^2 = \|\sqrt{\mathbf{D}}\nabla_h v\|^2 + \|\sqrt{\eta}[\![v]\!]\|_{\mathscr{F}_h^I \cup \mathscr{F}_h^D}^2, \qquad \forall v \in H^1(\mathscr{T}_h), \tag{11}$$

$$|||v|||_{\mathrm{DG}}^2 = \|v\|_{\mathrm{DG}}^2 + \|\eta^{-\frac{1}{2}}\{\!\{\mathbf{D}\nabla_h v\}\!\}\|_{\mathscr{F}_h^I \cup \mathscr{F}_h^D}^2, \quad \forall v \in H^2(\mathscr{T}_h). \tag{12}$$

Under Assumption 3.2, we recall that $|||v|||_{\mathrm{DG}}^2 \lesssim \|v\|_{\mathrm{DG}}^2$ for any $v \in W_h^{\mathrm{DG}}$, thanks to the trace-inverse inequality [18]. Moreover, we introduce the following proposition on the continuity and coercivity of the bilinear form [17, 18].

Proposition 3.3. Let Assumption 3.2 be satisfied, then the bilinear form $\mathscr{A}(\cdot,\cdot)$ is continuous and coercive (provided that the penalty parameter η is large enough):

$$|\mathscr{A}(v_h, w_h)| \lesssim \|v_h\|_{\mathrm{DG}}\|w_h\|_{\mathrm{DG}}, \quad \forall v_h, w_h \in W_h^{\mathrm{DG}}, \tag{13}$$

$$|\mathscr{A}(v_h, w_h)| \lesssim \|v_h\|_{\mathrm{DG}}|||w|||_{\mathrm{DG}}, \quad \forall v_h \in W_h^{\mathrm{DG}}, \forall w \in H^1(\mathscr{T}_h), \tag{14}$$

$$\|v_h\|_{\mathrm{DG}}^2 \lesssim \mathscr{A}(v_h, v_h) \qquad \forall v_h \in W_h^{\mathrm{DG}}. \tag{15}$$

Finally, we

Proposition 3.4 (Polynomial interpolant [24])**.** Let Assumption 3.1 be satisfied, then the following estimate holds:

$$\forall u \in H^n(\mathscr{T}_h) \;\; \exists u_I \in W_h^{\mathrm{DG}} : |||u - u_I|||_{\mathrm{DG}}^2 \lesssim \sum_{K \in \mathscr{T}_h} h_K^{2\min\{p+1,n\}-2}\|u\|_{H^n(K)}^2. \tag{16}$$

The interpolant u_I belongs to the discrete space, which means that it is a polynomial of order ℓ on each element K [22, §2.1]. This fact guarantees the boundedness in the L^∞-norm of the function u_I on a general polygonal element K for any t [25]:

$$\exists M_I > 0 : \|u_I\|_{L^\infty(\Omega)} \leq M_I \quad \forall t \in (0,T). \tag{17}$$

At the continous level, if the initial condition $c_0(\boldsymbol{x}) \in (0,1)$ and for homogeneous Neumann boundary conditions $\phi_N = 0$ and $f = 0$, then for each $(\boldsymbol{x},t) \in \Omega \times (0,T]$, we get that:

$$\|c(t)\|^2_{L^\infty(\Omega)} \leq 1 \quad \forall t \in (0,T). \tag{18}$$

4 Stability analysis of the SFK semi-discrete formulation

This section aims to derive a stability analysis for the solution of the PolyDG semi-discrete problem (10). Before that, we define the energy norm we are going to use for our study. The energy norm $\|\cdot\|_\varepsilon : H^1(\mathscr{T}_h) \to \mathbb{R}$ is defined as:

$$\|c_h(t)\|^2_\varepsilon = \|c_h(t)\|^2 + \int_0^t \|c_h(s)\|^2_{\mathrm{DG}}\, \mathrm{d}s + \int_0^t \|c_h(s)\|^3_{L^3(\Omega)}\, \mathrm{d}s. \tag{19}$$

Theorem 4.1 (Stability result)**.** *Let Assumptions 2.1 and 3.2 be satisfied. For a sufficiently large penalty coefficient η, let $\hat{c}_h(t)$ be the solution of Equation (10) for any $t \in (0,T]$. Then, the following estimates hold:*

$$\|\hat{c}_h(t)\|^2_\varepsilon \lesssim \|\hat{c}^0_h\|^2 + |\Omega| t + \int_0^t \|f(s)\|^2 \mathrm{d}s, \tag{20}$$

$$\|\hat{c}_h(t)\|^2_{\mathrm{DG}} + \|\hat{c}_h(t)\|^3_{L^3(\Omega)} \lesssim \|\hat{c}^0_h\|^2_{\mathrm{DG}} + \|\hat{c}^0_h\|^3_{L^3(\Omega)} + \|\hat{c}^0_h\|^2 t + |\Omega| t^2 + (1+t)\int_0^t \|f(s)\|^2 \mathrm{d}s., \tag{21}$$

where C_{E_2} is the constant coming from the discrete Sobolev-Poincaré inequality in [26].

Proof. **Proof of estimate (20).** Let us consider Equation (10) and choose $w_h = \hat{c}_h(s)$:

$$\left(\frac{\partial \hat{c}_h}{\partial t}, \hat{c}_h\right)_\Omega + \mathscr{A}(\hat{c}_h, \hat{c}_h) - \alpha(|\hat{c}_h|, \hat{c}_h)_\Omega + \alpha(|\hat{c}_h|, \hat{c}^2_h)_\Omega = F(\hat{c}_h).$$

After an integration in time in $(0,t)$ and using the coercivity estimate in (15) and the Hölder inequality on the forcing term we obtain:

$$\begin{aligned}\|\hat{c}_h(t)\|^2 + \int_0^t \left(\|\hat{c}_h(s)\|^2_{\mathrm{DG}} + \|\hat{c}_h(s)\|^3_{L^3(\Omega)}\right) \mathrm{d}s &\lesssim \|\hat{c}^0_h\|^2 + \int_0^t \left(\|\hat{c}_h(s)\|^2 + \|f(s)\|\|\hat{c}_h(s)\|\right) \mathrm{d}s \\ &\lesssim \|\hat{c}^0_h\|^2 + \int_0^t \left(\|\hat{c}_h(s)\|^2 + \|f(s)\|^2\right) \mathrm{d}s,\end{aligned}$$

where in the last step we used the Young inequality. The latter step that is needed is to bound the term $\|\hat{c}_h(s)\|^2$ on the right hand side. The latter can be rewritten using both Hölder and Young's inequalities:

$$\|\hat{c}_h\|^2 \leq \|\hat{c}_h\|^2_{L^3(\Omega)} |\Omega|^{\frac{1}{3}} \lesssim \|\hat{c}_h\|^3_{L^3(\Omega)} + |\Omega|,$$

where $|\Omega|$ denotes the measure of the domain. Substituting the result we obtain:

$$\|\hat{c}_h(t)\|_\varepsilon^2 \lesssim \|\hat{c}_h^0\|^2 + |\Omega|t + \int_0^t \|f(s)\|^2 \mathrm{d}s.$$

Proof of estimate (21). Let us consider Equation (10) and choose $w_h = \dot{\hat{c}}_h = \dfrac{\partial \hat{c}_h}{\partial t}$:

$$\|\dot{\hat{c}}_h\|^2 + \mathscr{A}(\hat{c}_h, \dot{\hat{c}}_h) - \alpha(|\hat{c}_h|, \dot{\hat{c}}_h)_\Omega + \alpha(|\hat{c}_h|\hat{c}_h, \dot{\hat{c}}_h)_\Omega = F(\dot{\hat{c}}_h).$$

We can observe that due to the symmetry of $\mathscr{A}$:

$$\begin{aligned}
\int_0^t \mathscr{A}(\hat{c}_h(s), \dot{\hat{c}}_h(s))\mathrm{d}s &= \frac{1}{2}\mathscr{A}(\hat{c}_h(t), \hat{c}_h(t)) - \frac{1}{2}\mathscr{A}(\hat{c}_h^0, \hat{c}_h^0), \\
\int_0^t \alpha(|\hat{c}_h(s)|\hat{c}_h(s), \dot{\hat{c}}_h(s))_\Omega &= \frac{\alpha}{3}\|\hat{c}_h(t)\|_{L^3(\Omega)}^3 - \frac{\alpha}{3}\|\hat{c}_h^0\|_{L^3(\Omega)}^3.
\end{aligned}$$

Then, after an integration in time in $(0, t)$ and using the coercivity and continuity estimates in (15) and (13) we obtain:

$$\begin{aligned}
&\|\hat{c}_h(t)\|_{\mathrm{DG}}^2 + \|\hat{c}_h(t)\|_{L^3(\Omega)}^3 + \int_0^t \|\dot{\hat{c}}_h(s)\|^2 \mathrm{d}s \\
&\quad\lesssim \|\hat{c}_h^0\|_{\mathrm{DG}}^2 + \|\hat{c}_h^0\|_{L^3(\Omega)}^3 + \int_0^t (|\hat{c}_h(s)|, \dot{\hat{c}}_h(s))_\Omega \mathrm{d}s + \int_0^t (f(s), \dot{\hat{c}}_h(s))_\Omega \mathrm{d}s \\
&\quad\lesssim \|\hat{c}_h^0\|_{\mathrm{DG}}^2 + \|\hat{c}_h^0\|_{L^3(\Omega)}^3 + \int_0^t \left(\|\hat{c}_h(s)\|^2 + \|f(s)\|^2 + \|\dot{\hat{c}}_h(s)\|^2 \right) \mathrm{d}s,
\end{aligned}$$

where in the last steps we used the Hölder and Young inequalities. After simplification of $\|\dot{\hat{c}}_h(s)\|^2$, we use the stability estimate (20) to bound $\|\hat{c}_h(s)\|$ on the right hand side:

$$\|\hat{c}_h(t)\|_{\mathrm{DG}}^2 + \|\hat{c}_h(t)\|_{L^3(\Omega)}^3 \mathrm{d}s \lesssim \|\hat{c}_h^0\|_{\mathrm{DG}}^2 + \|\hat{c}_h^0\|_{L^3(\Omega)}^3 + t\|\hat{c}_h^0\|^2 + |\Omega|t^2 + (1+t)\int_0^t \|f(s)\|^2 \mathrm{d}s.$$

□

Remark 4.2. The stability estimates (20) and (21) are established for general polygonal and polyhedral meshes satisfying Assumption 3.2, in the spirit of [18]. This represents a substantial advance over the stability analysis for the FK model in [13], which relied on the more restrictive Assumption 3.1. In addition, the stability result for the SFK model is global in time, and the dependence on the final time t in the energy norm is linear rather than exponential as in [13], ensuring significantly better control for large times. The analysis can be extended to full Neumann boundary conditions by using the Sobolev-Poincaré-Wirtinger inequality from [26], without loss of generality. ∎

Remark 4.3. Under the assumption of $f = 0$, the stability estimate (20) of Theorem 4.1 becomes:

$$\|\hat{c}_h(t)\|_\varepsilon^2 \lesssim \|\hat{c}_h^0\|^2 + |\Omega|t = \hat{C}_S(\hat{c}_h^0, |\Omega|, t), \tag{22}$$

while the stability estimate (21) reduces to:

$$\|\hat{c}_h(t)\|_{\mathrm{DG}}^2 + \|\hat{c}_h(t)\|_{L^3(\Omega)}^3 \lesssim \|\hat{c}_h^0\|_{\mathrm{DG}}^2 + \|\hat{c}_h^0\|_{L^3(\Omega)}^3 + t\|\hat{c}_h^0\|^2 + |\Omega|t^2 = \widetilde{C}_S(\hat{c}_h^0, |\Omega|, t). \tag{23}$$

The definitions of $\hat{C}_S$ and $\widetilde{C}_S$ will be used in the following analysis.

5 *A-priori* error analysis of the SFK semi-discrete formulation

In this section, we derive an *a-priori* error estimate for the solution of the semi-discrete PolyDG formulation (10). We assume homogeneous forcing term $f = 0$ and full Neumann boundary conditions, i.e. $\phi_N = 0$, respectively.

Theorem 5.1. *Consider problem (9) with $f = 0$, $\phi_N = 0$ for $\Gamma_N = \partial\Omega$. Let Assumptions 2.1 and 3.2 be valid and let $\hat{c}$ be the weak solution of (9) for any $t \in (0, T]$ and let it satisfy the following additional regularity requirement:*

$$\hat{c} \in C^1((0,T]; H^n(\Omega) \cap L^\infty(\Omega)), \tag{24}$$

where $n \geq 2$. Let also assume further regularity on the initial condition $c_0 \in W_0$. For a sufficiently large penalty coefficient η, let $\hat{c}_h$ be the solution of (10) for any $t \in (0, T]$. Then, for any $t \in (0, T]$ it holds:

$$\begin{aligned}\|\hat{c}(t) - \hat{c}_h(t)\|^2 + \int_0^t |||\hat{c}(s) - \hat{c}_h(s)|||^2_{\mathrm{DG}} \mathrm{d}s \lesssim & \sum_{K\in\mathscr{T}_h} h_K^{2min\{p+1,n\}-2} \|\hat{c}(t)\|^2_{H^n(K)} \\ & + \sum_{K\in\mathscr{T}_h} h_K^{2min\{p+1,n\}-2} \int_0^t \left(\|\dot{\hat{c}}(s)\|^2_{H^n(K)} + \|\hat{c}(s)\|^2_{H^n(K)}\right) \mathrm{d}s,\end{aligned} \tag{25}$$

provided $\mu \gtrsim \alpha$, where the hidden constant depends on the interpolation constant M_I of equation (17), the stability constant $\widetilde{C}_S$ defined in equation (23) and the discrete Sobolev embedding constant C_{E_q} for the $L^q(\Omega)$ spaces in [26].

Proof. We subtract equation (10) from the weak formulation of (9) to obtain:

$$\left(\dot{\hat{c}} - \dot{\hat{c}}_h, w_h\right)_\Omega + \mathscr{A}\left(\hat{c} - \hat{c}_h, w_h\right) - \alpha\left(|\hat{c}| - |\hat{c}_h|, w_h\right)_\Omega + \alpha\left(\hat{c}|\hat{c}| - \hat{c}_h|\hat{c}_h|, w_h\right)_\Omega = 0 \quad \forall w_h \in W_h^{\mathrm{DG}}.$$

Then, we define the errors $\hat{e}_h^c = c_I - \hat{c}_h$ ed $e_I^c = \hat{c} - c_I$, with c_I being a suitable interpolant. By setting $w_h = \hat{e}_h^c$:

$$\left(\dot{\hat{e}}_h^c, \hat{e}_h^c\right)_\Omega + \mathscr{A}\left(\hat{e}_h^c, \hat{e}_h^c\right) - \alpha\left(|\hat{c}| - |\hat{c}_h|, \hat{e}_h^c\right)_\Omega + \alpha\left(\hat{c}|\hat{c}| - \hat{c}_h|\hat{c}_h|, \hat{e}_h^c\right)_\Omega = \left(\dot{e}_I^c, \hat{e}_h^c\right)_\Omega + \mathscr{A}\left(e_I^c, \hat{e}_h^c\right).$$

We remark that $\hat{e}_h^c(0) = 0$ by setting $\hat{c}_h^0 = c_I(0)$ and, by using the symmetry of the scalar product,

$$\left(\dot{\hat{e}}_h^c, \hat{e}_h^c\right)_\Omega = \frac{1}{2}\frac{\mathrm{d}}{\mathrm{d}t}\left(\hat{e}_h^c, \hat{e}_h^c\right)_\Omega = \frac{1}{2}\frac{\mathrm{d}}{\mathrm{d}t}\|\hat{e}_h^c\|^2.$$

We integrate in time between 0 and a generic time instant t such that:

$$\begin{aligned}\|\hat{e}_h^c(t)\|^2 + \int_0^t \|\hat{e}_h^c(s)\|^2_{\mathrm{DG}}\, \mathrm{d}s = & \int_0^t (\dot{e}_I^c(s), \hat{e}_h^c(s))_\Omega \mathrm{d}s + \int_0^t \mathscr{A}(e_I^c(s), \hat{e}_h^c(s)) \mathrm{d}s \\ & + \int_0^t \left(|\hat{c}(s)| - |\hat{c}_h(s)|, \hat{e}_h^c(s)\right)_\Omega \mathrm{d}s + \int_0^t \left(\hat{c}(s)|\hat{c}(s)| - \hat{c}_h(s)|\hat{c}_h(s)|, \hat{e}_h^c(s)\right)_\Omega \mathrm{d}s\end{aligned}$$

Now, we can use Equation (13) and Hölder inequality to obtain

$$\begin{aligned}\|\hat{e}_h^c(t)\|^2 + \int_0^t \mu \|\hat{e}_h^c(s)\|^2_{\mathrm{DG}}\, \mathrm{d}s \lesssim & \int_0^t \|\dot{e}_I^c(s)\| \, \|\hat{e}_h^c(s)\| \mathrm{d}s + \int_0^t |||e_I^c(s)|||_{\mathrm{DG}} \, \|\hat{e}_h^c(s)\|_{\mathrm{DG}} \mathrm{d}s \\ & + \int_0^t \alpha \underbrace{\left(|\hat{c}(s)| - |\hat{c}_h(s)|, \hat{e}_h^c(s)\right)_\Omega}_{(1)} \mathrm{d}s + \int_0^t \alpha \underbrace{\left(\hat{c}(s)|\hat{c}(s)| - \hat{c}_h(s)|\hat{c}_h(s)|, \hat{e}_h^c(s)\right)_\Omega}_{(2)} \mathrm{d}s\end{aligned} \tag{26}$$

The integrand (1) can be bounded by combining the triangular and Cauchy-Schwarz inequalities:

$$\begin{aligned}(|\hat{c}|-|\hat{c}_h|,\hat{e}_h^c)_\Omega &= \int_\Omega (|\hat{c}|-|\hat{c}_h|)\hat{e}_h^c \le \int_\Omega ||\hat{c}|-|\hat{c}_h||\ |\hat{e}_h^c| \le \int_\Omega |\hat{c}-\hat{c}_h|\,|\hat{e}_h^c| \\ &= \int_\Omega |\underbrace{\hat{c}-c_I}_{=e_I^c}+\underbrace{c_I-\hat{c}_h}_{=\hat{e}_h^c}|\,|\hat{e}_h^c| \le \int_\Omega (|e_I^c|+|\hat{e}_h^c|)|\hat{e}_h^c| \le \|e_I^c\|\ \|\hat{e}_h^c\|+\|\hat{e}_h^c\|^2.\end{aligned}$$

Moreover, the integrand denoted by (2) can be manipulated as follows:

$$\begin{aligned}\hat{c}|\hat{c}|-\hat{c}_h|\hat{c}_h| &= \hat{c}|\hat{c}|-\hat{c}|c_I|+\hat{c}|c_I|-c_I|c_I|+c_I|c_I|-|c_I|\hat{c}_h+|c_I|\hat{c}_h-|\hat{c}_h|\hat{c}_h \\ &= \underbrace{\hat{c}(|\hat{c}|-|c_I|)}_{\text{(I)}}+\underbrace{|c_I|(\hat{c}-c_I)}_{\text{(II)}}+\underbrace{|c_I|(c_I-\hat{c}_h)}_{\text{(III)}}+\underbrace{\hat{c}_h(|c_I|-|\hat{c}_h|)}_{\text{(IV)}}.\end{aligned}$$

Each resulting term can be treated in the following way:

- The term (I) can be bounded using the triangular and Cauchy-Schwarz inequalities and the bound of continuous solution (18):

$$|(\mathrm{I})| \le |(\hat{c}(|\hat{c}|-|c_I|),\hat{e}_h^c)_\Omega| \le \|\hat{c}\|_{L^\infty(\Omega)}\|\hat{c}-c_I\|\,\|\hat{e}_h^c\| \le \|e_I^c\|\,\|\hat{e}_h^c\|.$$

- The term (II) can be bounded using the Cauchy-Schwarz inequality and the interpolant bound (17):

$$|(\mathrm{II})| \le |(|c_I|(\hat{c}-c_I),\hat{e}_h^c)_\Omega| \le \|c_I\|_{L^\infty(\Omega)}\|\hat{c}-c_I\|\,\|\hat{e}_h^c\| \le M_I\|e_I^c\|\,\|\hat{e}_h^c\|.$$

- The term (III) can be bounded using the Cauchy-Schwarz inequality, the bound of interpolant (17), and the Sobolev-Poincaré-Wirtinger inequality with constant C_{E_2} [26]:

$$|(\mathrm{III})| \le |(|c_I|(c_I-\hat{c}_h),\hat{e}_h^c)_\Omega| \le \|c_I\|_{L^\infty(\Omega)}\|\hat{e}_h^c\|^2 \le M_I C_{E_2}\|\hat{e}_h^c\|_{\mathrm{DG}}^2.$$

- The term (IV) can be bounded using the stability estimate of the $L^3(\Omega)$-norm of the solution (23), the triangular, Hölder, and the Sobolev-Poincaré-Wirtinger inequality with constant C_{E_3}[26]:

$$|(\mathrm{IV})| \le |(\hat{c}_h(|c_I|-|\hat{c}_h|),\hat{e}_h^c)_\Omega| \le \left|\left(\hat{c}_h,(\hat{e}_h^c)^2\right)_\Omega\right| \le \|\hat{c}_h\|_{L^3(\Omega)}\|\hat{e}_h^c\|_{L^3(\Omega)}^2 \le \widetilde{C}_S C_{E_3}\|\hat{e}_h^c\|_{\mathrm{DG}}^2.$$

Then, Equation (26) using the equivalence of the DG-norms in W_h^{DG} and provided $\mu \gtrsim \alpha$ becomes:

$$\|\hat{e}_h^c(t)\|^2+\int_0^t |||\hat{e}_h^c(s)|||_{\mathrm{DG}}^2\ \mathrm{d}s \lesssim \int_0^t (\|\dot{e}_I^c(s)\|+\|e_I^c(s)\|)\,\|\hat{e}_h^c(s)\|\mathrm{d}s+\int_0^t |||e_I^c(s)|||_{\mathrm{DG}}\|\hat{e}_h^c(s)\|_{\mathrm{DG}}\mathrm{d}s.$$

Using once again Hölder inequality, Grönwall's lemma [27] and the estimate in (16), we obtain:

$$\begin{aligned}\|\hat{e}_h^c(t)\|^2+\int_0^t |||\hat{e}_h^c(s)|||_{\mathrm{DG}}^2\ \mathrm{d}s &\lesssim \int_0^t \left(\|\dot{e}_I^c(s)\|^2+\|e_I^c(s)\|^2+\|e_I^c(s)\|_{\mathrm{DG}}^2\right)\mathrm{d}s \\ &\lesssim \sum_{K\in\mathscr{T}_h} h_K^{2\min\{p+1,n\}-2}\int_0^t \left(\|\dot{\hat{c}}(s)\|_{H^n(K)}^2+\|\hat{c}(s)\|_{H^n(K)}^2\right)\ \mathrm{d}s.\end{aligned}$$

Finally, using the triangular inequality, we find the thesis. □

Remark 5.2. Given Proposition 3.4, we assume that in problem (10) the initial condition is $c_h^0 = c_I(0) \in W_h^{\mathrm{DG}}$, with $c_0 = c_0(\boldsymbol{x})$ being sufficiently regular, i.e. $c_0 \in W_D$. Moreover, we require element-wise H^2-

regularity of the concentration together with the continuity of the flux through the interfaces $F \in \mathscr{F}_h^I$ for $t > 0$, because we want to extend the bilinear forms of (10) to the space of continuous solutions. ∎

6 Fully-discrete SFK formulation

Let $\{\varphi_j\}_{j=0}^N$ be a suitable basis for W_h^{DG}, where N is the dimension of the space W_h^{DG}. Then, $\hat{c}_h(t) = \sum_{j=0}^{N} C_j(t)\varphi_j$ and we denote by $\mathbf{C} \in \mathbb{R}^N$ the corresponding vector of expansion coefficients in the chosen basis. We define the following matrices $\forall i, j = 1, ..., N$:

$$[\mathbf{M}]_{ij} = (\varphi_j, \varphi_i)_\Omega, \quad \text{(Mass matrix)} \qquad [\mathbf{A}]_{ij} = \mathscr{A}(\varphi_j, \varphi_i) \quad \text{(Stiffness matrix)}$$

$$[\mathbf{R}(\mathbf{C}(t))]_{ij} = (\alpha|\hat{c}_h(t)|, \varphi_i)_\Omega, \quad \text{(Reaction matrix)} \qquad [\widetilde{\mathbf{R}}(\mathbf{C}(t))]_{ij} = (\alpha|\hat{c}_h(t)|\varphi_j, \varphi_i)_\Omega. \quad \text{(Reaction matrix)}$$

Moreover, we define the forcing term $[\mathbf{F}]_j = F(\varphi_j) = (f, \varphi_j)_\Omega \ \forall j = 1, ..., N$. Then problem (10) can be written as:

$$\mathbf{M}\dot{\mathbf{C}}(t) + \mathbf{A}\mathbf{C}(t) - \mathbf{R}(\mathbf{C}(t)) + \widetilde{\mathbf{R}}(\mathbf{C}(t))\mathbf{C}(t) = \mathbf{F}(t), \quad \forall t \in (0, T] \tag{27}$$

$$\mathbf{C}(0) = \mathbf{C}^0. \tag{28}$$

We define a partition of the time interval $[0, T]$ into N_T subintervals $[t_n, t_{n+1}] \ \forall n = 0, ..., N_T - 1$, with $\Delta t = t_{n+1} - t_n$. We employ the Crank-Nicolson scheme such that the fully-discrete formulation reads: Given $\mathbf{C}(0) = \mathbf{C}^0$, $\forall n = 0, ..., N_T - 1$, find $\mathbf{C}^{n+1} \simeq \mathbf{C}(t_{n+1})$ such that:

$$\mathbf{M}\mathbf{C}^{n+1} + \frac{\Delta t}{2}(\mathbf{A} + \widetilde{\mathbf{R}}(\mathbf{C}^*))\mathbf{C}^{n+1} = \mathbf{M}\mathbf{C}^n - \frac{\Delta t}{2}(\mathbf{A} + \widetilde{\mathbf{R}}(\mathbf{C}^*))\mathbf{C}^n + \Delta t\ \mathbf{R}(\mathbf{C}^*) + \frac{\Delta t}{2}(\mathbf{F}^n + \mathbf{F}^{n+1}), \tag{29}$$

where we use a semi-implicit treatment of the nonlinearity $\mathbf{C}^* = \frac{3}{2}\mathbf{C}^n - \frac{1}{2}\mathbf{C}^{n-1}$.

7 Verification of the SFK model

In this section, we verify the theoretical results by performing a convergence study based on a manufactured solution in both two-dimensional (2D) and three-dimensional (3D) settings.

7.1 Test Case 1: verification of 2D convergence

We design a convergence test to verify the theoretical bounds derived in the previous sections. For the 2D numerical tests, we use a MATLAB library called `lymph` [28], which implements the SFK solver on polygonal meshes. We consider a unit square domain $\Omega = (0, 1)^2$ and the corresponding mesh has been generated with PolyMesher [29]. In this test, the manufactured solution is given by:

$$\hat{c}(x, y, t) = \frac{1}{4}\left(\cos(\pi x)\cos(\pi y) + 2\right) e^{-t}.$$

To simplify the problem, we assume isotropic diffusion, i.e. $\mathbf{D} = \mathbf{I}$, which yields $\alpha = 1$ and $\eta_0 = 10$. The forcing term f and the boundary conditions are constructed from the exact solution. We employ a fixed timestep $\Delta t = 10^{-5}$ and final time $T = 10^{-3}$ for both h- and p-convergence studies. For the h-convergence analysis, we consider four meshes with $N_{\mathrm{el}} = 30, 100, 300, 1000$ elements and polynomial degrees $p = 1, \ldots, 6$. For the p-convergence study, we fix the mesh with $N_{\mathrm{el}} = 30$ elements and vary the polynomial degree in the range $p = 1, \ldots, 8$.

Figure 1 displays the errors at final time T as functions of the mesh size for polynomial degrees $p = 1, \ldots, 6$, measured in both the L^2-norm and the DG-norm. The observed convergence rates are

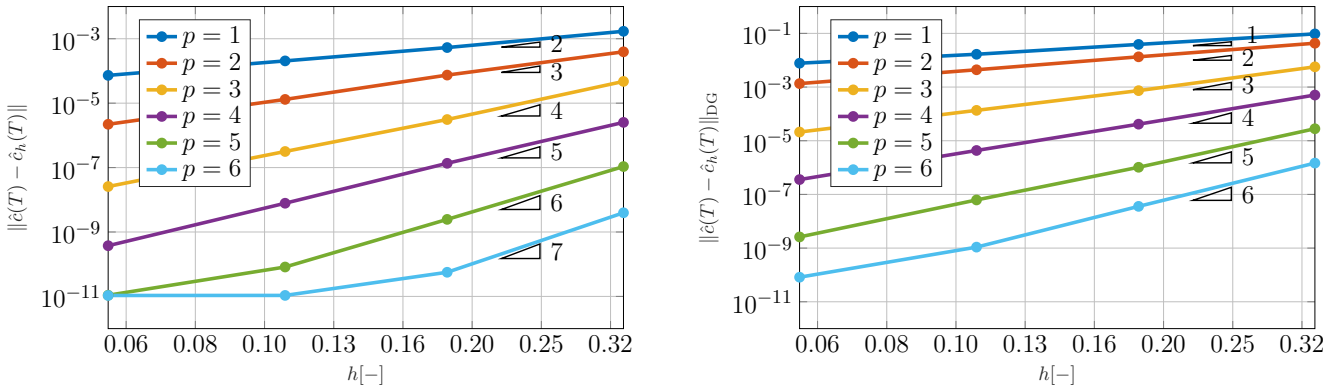

Figure 1 Test Case 1: computed errors and convergence rates with $L2$-norm (left) and DG-norm (right).

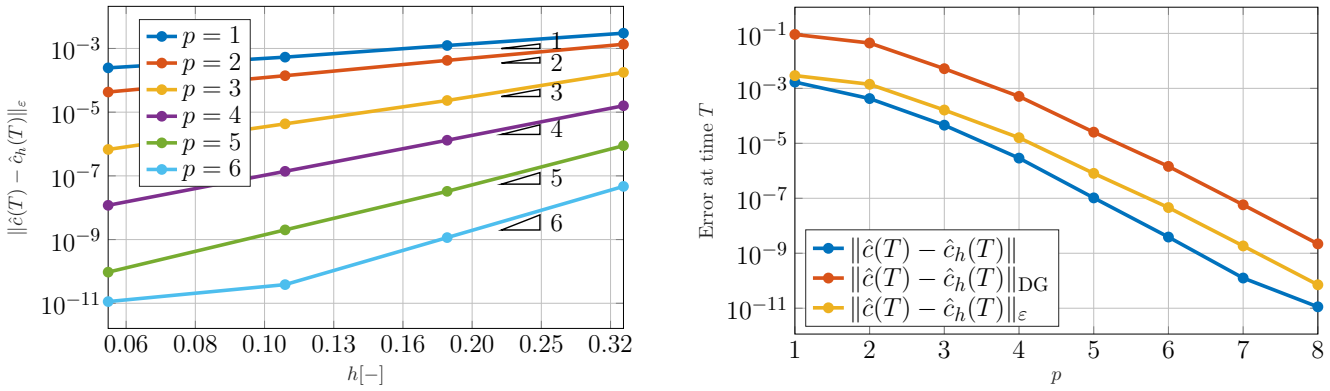

Figure 2 Test Case 1: computed errors in the energy norm (left) and convergence w.r.t. to the p (right).

consistent with Theorem 5.1: we recover order p in the DG-norm and order $p+1$ in the L^2-norm. Although the latter is not covered by the present theoretical analysis, optimal rates are clearly observed in practice.

Figure 2 (left) reports the errors measured in the energy norm defined in (19), confirming the expected order p convergence under mesh refinement. On the right, we present the p-convergence results on the mesh with $N_{\mathrm{el}} = 30$, measured in the L^2-, DG-, and energy norms. In this case, the errors exhibit exponential decay with respect to the polynomial degree p, indicating numerically optimal behavior despite the lack of a corresponding theoretical estimate.

7.2 Test Case 2: verification of 3D convergence

In this section, we extend the convergence study of the SFK model to the 3D case. The simulation of this section have been carried out with `Vulpes` (Versatile and parallel compUtational Library for high-order discontinuous Polytopal Element Simulations) [30], an open-source and general-purpose C++ library developed for the numerical solution of multiphysics and multiscale differential problems.

We consider a cubic domain $\Omega = (0,1)^3$. The manufactured solution of the problem is given by:

$$\hat{c}(x,y,z,t) = (\sin(\pi x)\sin(\pi y)\sin(\pi z) + 2)e^{-t}.$$

We assume isotropic diffusion, which means $\mathbf{D} = \mathbf{I}$, $\alpha = 0.1$ and $\eta_0 = 10$. The forcing term f and the boundary conditions on $\partial\Omega$ are derived accordingly to the exact solution. We use a fixed timestep $\Delta t = 10^{-8}$ and a final time of simulation $T = 10^{-6}$ for both h-convergence and p-convergence studies. For the h-convergence study, we select five meshes with $h = 0.45, 0.35, 0.279, 0.226, 0.17479$ respectively

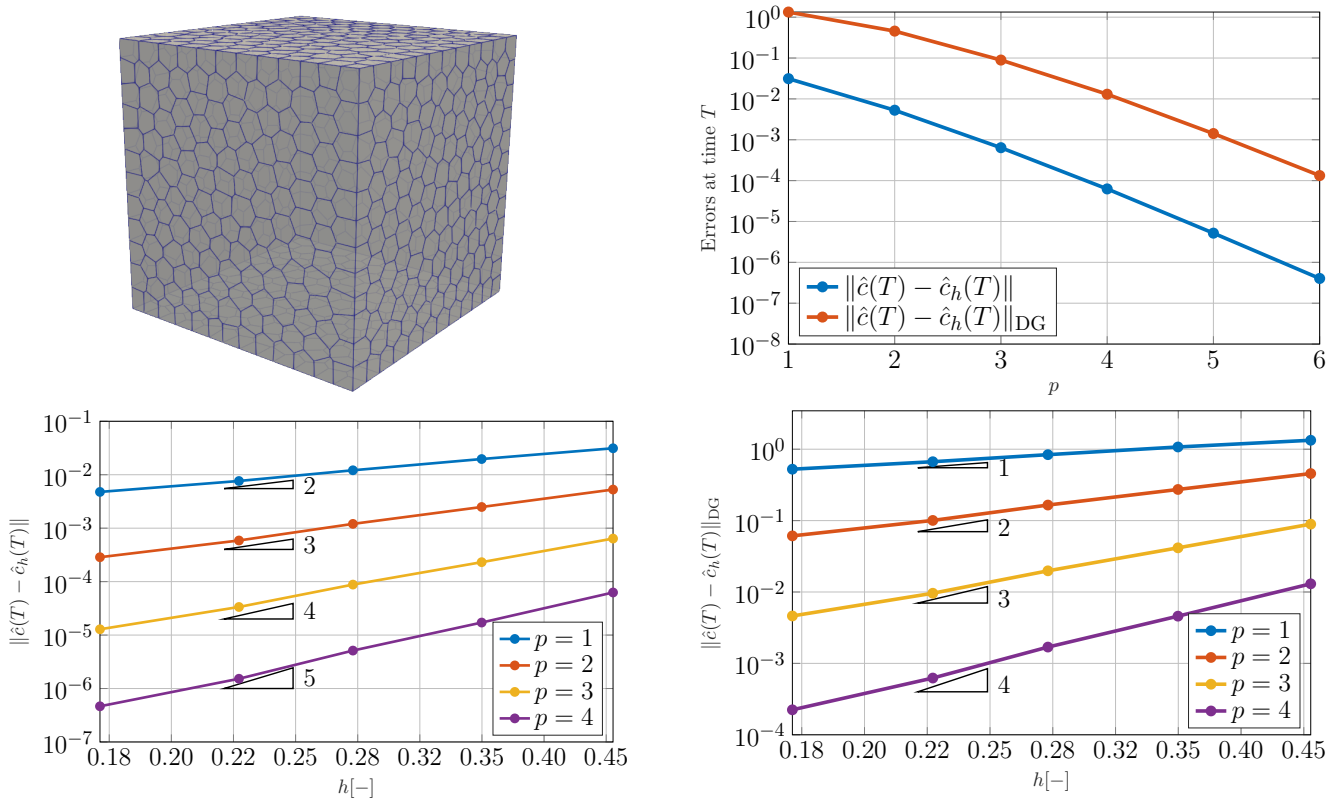

Figure 3 Test Case 2: example of a Voronoi grid used (top-left) and computed errors with respect to different polynomial degrees (top-right). Computed errors and convergence rates in the L^2-norm (bottom-left) and DG-norm (bottom-right).

generated via `Voro++` [31] and we repeat the simulation for polynomial degrees $p = 1, \dots, 4$.

The second row of Figure 3 shows the computed errors at final time T versus the mesh size for each polynomial degree in the L^2-norm and DG-norm, respectively. We observe that the expected convergence rates are obtained as claimed in Theorem 5.1.

For the p-convergence study, we use different polynomial degrees $p = 1, ..., 6$ on the mesh with $h = 0.45$. Figure 3 (top-right) shows the results of this analysis. We notice an exponential decay of the errors with respect to the polynomial degree p, which confirms that optimal convergence is achieved. As already explained in the 2D case, there is no theoretical estimate that validates this experimental behaviour.

8 Validation of the SFK model

In this section, we validate the SFK model through simulations of realistic problems and compare its performance with that of the FK model.

8.1 Test case 3: comparison of the FK and SFK models for a two-dimensional traveling wave

In this section, we use the PolyDG formulation to simulate the travelling-wave solution of the FK equation in two dimensions. We consider a solution of the form $c(x, y, t) = \psi(x - vt) = \psi(\xi)$. By substituting the expression into problem (1) with homogeneous forcing term $f = 0$ and free boundary conditions, we

obtain the following system of equations:

$$\begin{aligned} \chi'(\xi) &= -\frac{v}{d_{ext}}\chi(\xi) + \frac{1}{d_{ext}}\psi(\xi)(1-\psi(\xi)), \qquad \xi \in (0,T], \\ \psi'(\xi) &= \chi(\xi), \qquad \xi \in (0,T], \end{aligned} \tag{30}$$

assuming an isotropic diffusion tensor $\mathbf{D} = d_{ext}\mathbf{I}$. For this test case, we use the parameters $d_{ext} = 10^{-3}$, $\alpha = 1$, and $\eta_0 = 10$. The wave speed is set to $v = 0.1$, with initial conditions $\psi(0) = 1$ and $\chi(0) = -10^{-2}$. The chosen parameters are taken from [13] to allow a direct comparison between the proposed model and the reference. We consider two final simulation times, $T = 5$ and $T = 10$ and $\Omega = (0,5) \times (0,1)$. We compute a reference solution of problem (30) numerically using MATLAB's `ode45` solver, with a tolerance set to 10^{-12}.

First, we analyze the effect of different mesh sizes ($N_{\text{el}} = 30, 100, 300$), keeping the time step fixed at $\Delta t = 0.01$, and compute the L^2-error at the final simulation time for both $p = 2$ and $p = 3$. The results are reported in Table 1 for both the FK and SFK methods. We observe that the stabilized version significantly reduces the errors, particularly for coarse meshes with a lower number of degrees of freedom. Remarkably, our model is able to simulate the traveling wave even for $p = 1$. In Figure 4, where we display the solutions at the final simulation time for both methods. For $T = 10$, the solutions produced by the original model are completely unreliable, whereas our formulation provides reasonably accurate results in all cases. The numerical scheme proposed in [13] lacks robustness when the solution approaches negative values, due to the instability of the equilibrium point at $c = 0$.

Figure 5 illustrates an example where the error-correction mechanism is active. We report the solution along the line $y = 0.5$ for $x \in [0,5]$, with $p = 2$ and $N_{\text{el}} = 30$, using both schemes. For the positivity-preserving scheme, when the solution reaches negative values, the model corrects the oscillations after few iterations. In contrast, the scheme without positivity preservation amplifies the oscillations around $c = 0$, leading to the results shown in Figure 4. Additionally, with the classical formulation we observe oscillations also around $c = 1$, which are typical in applications with fast variations (high gradients), in addition to those occurring at $c = 0$. As shown, our method is able to damp the oscillations at $c = 1$ as well, leading to overall improved results.

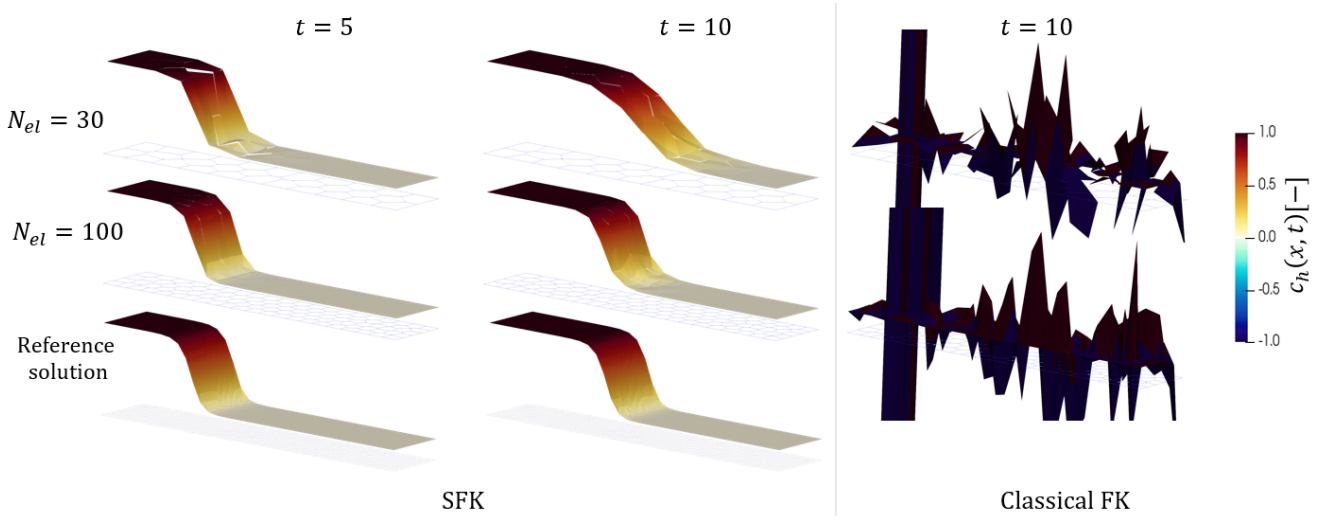

Figure 4 Test case 3: solutions with different mesh refinements using both the classical and stabilized FK formulations with $p = 2$.

In Figure 6, the left panel reports the error in the energy norm for three polynomial orders as a function of time. The behavior for $p = 2$ is qualitatively consistent with the other cases, further supporting the

Table 1 Test case 3: computed L^2 errors at final time with different mesh refinements ($\Delta t = 0.01$): $p = 2$ (top) and $p = 3$ (bottom) for SFK and Classical FK formulations.

		SFK		**FK** [13]			
		Semi-Implicit		Semi-Implicit		Implicit	
Refinement	DOFs	$T = 5$	$T = 10$	$T = 5$	$T = 10$	$T = 5$	$T = 10$
				$p = 2$ $\Delta t = 0.01$			
$N_{el} = 30$	180	7.00×10^{-2}	4.74×10^{-1}	6.33×10^{2}	1.03×10^{4}	1.63×10^{9}	5.36×10^{6}
$N_{el} = 100$	600	5.55×10^{-3}	8.72×10^{-2}	1.45×10^{2}	1.12×10^{4}	8.24×10^{-1}	2.18×10^{7}
$N_{el} = 300$	1800	3.00×10^{-3}	3.70×10^{-3}	1.98×10^{1}	6.02×10^{4}	6.97×10^{-2}	1.28×10^{8}
				$p = 3$ $\Delta t = 0.01$			
$N_{el} = 30$	300	1.41×10^{-2}	2.81×10^{-1}	9.27×10^{-1}	6.75×10^{4}	1.56×10^{-1}	7.34×10^{7}
$N_{el} = 100$	1000	2.70×10^{-3}	6.20×10^{-3}	5.50×10^{-2}	7.20×10^{-1}	8.12×10^{-3}	1.78×10^{-1}
$N_{el} = 300$	3000	2.70×10^{-3}	5.90×10^{-3}	6.35×10^{-4}	7.80×10^{-3}	7.71×10^{-4}	2.12×10^{-3}

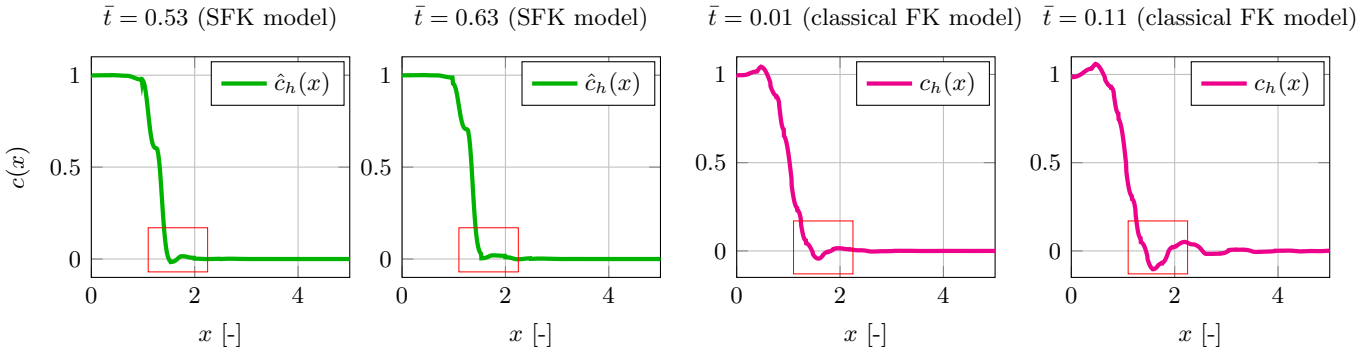

Figure 5 Test case 3: snapshots of the approximated solution along the line $y = 0.5$ at different timestamps for the SFK model and the classical FK model [13].

improved long-time stability predicted by Theorem 4.1. In particular, no exponential growth is observed for low-order approximations, in contrast with the formulation in [13]. The right panel shows the error at the final time $T = 5$ as a function of the number of degrees of freedom (DOFs), comparing h-refinement with fixed polynomial order $p = 2$ and p-refinement on a fixed mesh with $N_{\text{el}} = 30$. For a fixed number of DOFs, higher polynomial orders consistently yield lower errors than mesh refinement, indicating that p-refinement is more effective than h-refinement in this setting.

8.2 Test Case 4: Spreading of α-synuclein in a 2D brain section

In this section, we simulate the spreading of α-synuclein protein on a polygonal agglomerated grid representing a brain section. We use an agglomerated mesh made of 534 elements that represents a sagittal brain slice (see [32, Fig. 6b] for details about mesh and axonal fibres). The solution is computed by using a polynomial order of discretization $p = 4$ and a timestep $\Delta t = 10^{-2}$ years. Concerning the parameters of the model, we select an extracellular diffusion magnitude $d_{ext} = 8$ mm^2/year and an axonal diffusion magnitude $d_{axn} = 80$ mm^2/year [33]. Moreover, we set the reaction parameter $\alpha = 0.9$/year and the penalty coefficient $\eta_0 = 10$. We assume $f = 0$ and impose homogeneous Neumann boundary conditions on $\partial\Omega$. As initial condition, we consider a Gaussian concentration of proteins initially located in the dorsal motor nucleus [20].

In Figure 7, we report the initial condition and the solution at different time instants up to the final

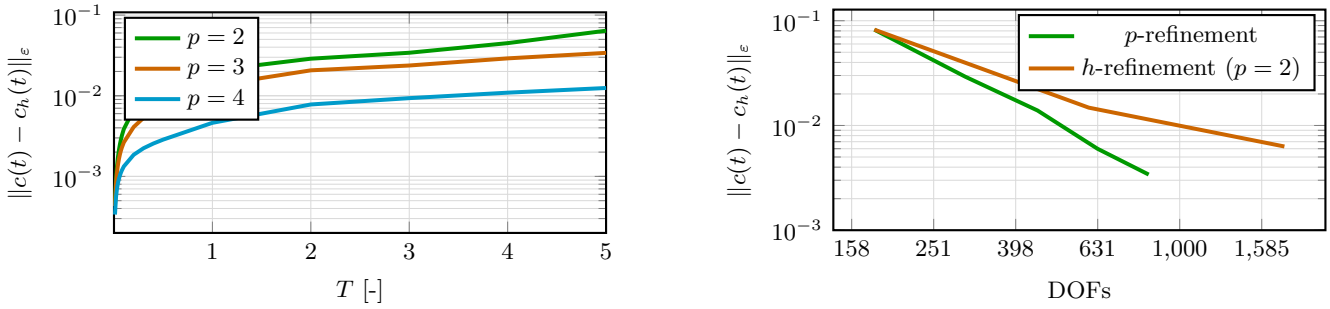

Figure 6 Test case 3: computed errors with respect to the simulation time T for $N_{el} = 30$ (left) and with respect to the number of degrees of freedom (DOFs) considering p-refinement and h-refinement (right).

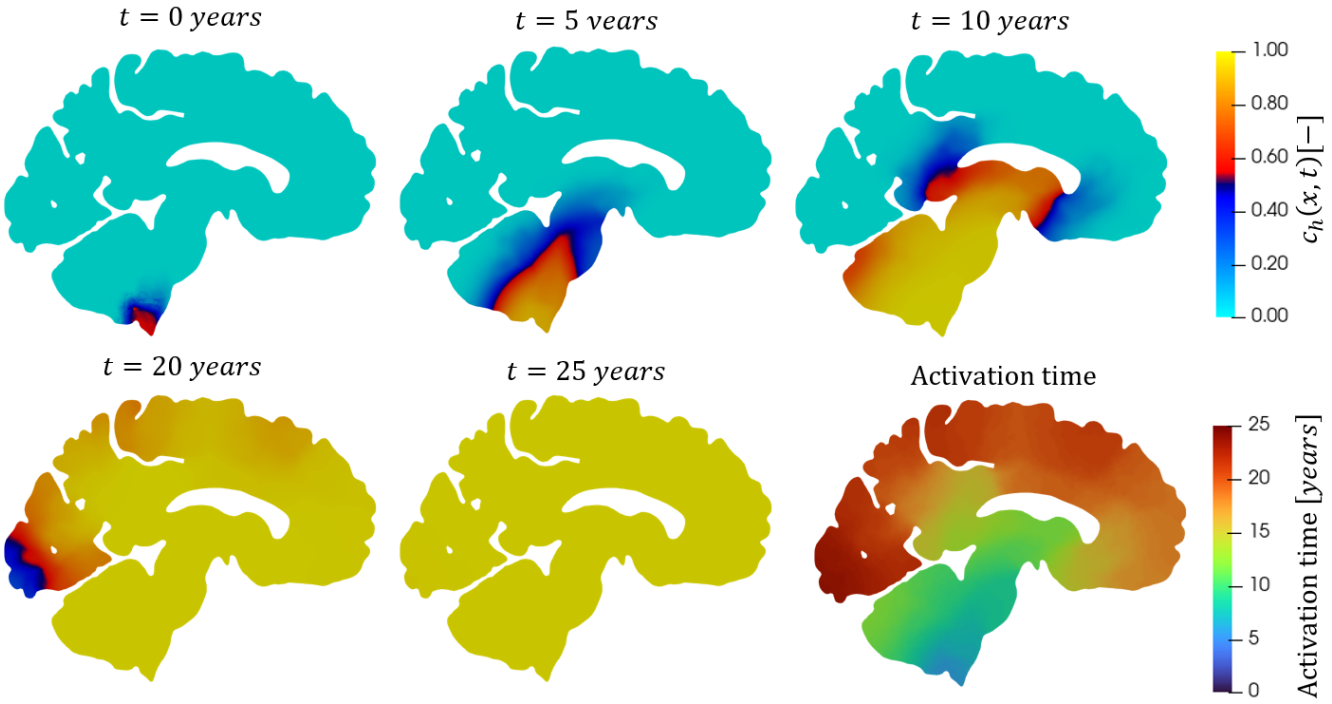

Figure 7 Test Case 4: patterns of computed α-synuclein concentration $\hat{c}_h$ through different years of development of the pathology and corresponding activation time computed with the SFK model and polynomial order $p = 4$.

time $T = 25$ years. We observe that the diffusion of the misfolded proteins is coherent with the medical literature [20, 21]. We highlight that the time development of the pathology is of the order of 25 years, coherently with the medical literature. Furthermore, we compute the activation time of the pathology as:

$$\hat{t}(\boldsymbol{x}) = \underset{t \in (0,T]}{\operatorname{argmin}} \{\hat{c}_h(\boldsymbol{x}, t) \geq c_{\text{crit}}\} \tag{31}$$

where we set the critical concentration of misfolded proteins $c_{\text{crit}} = 0.95$. The choice of this value is justified by the fact that higher values of concentration of proteins compromise the electric signal transport. The activation time gives us the idea of the time after which a neuron is damaged due to the progression of the disease.

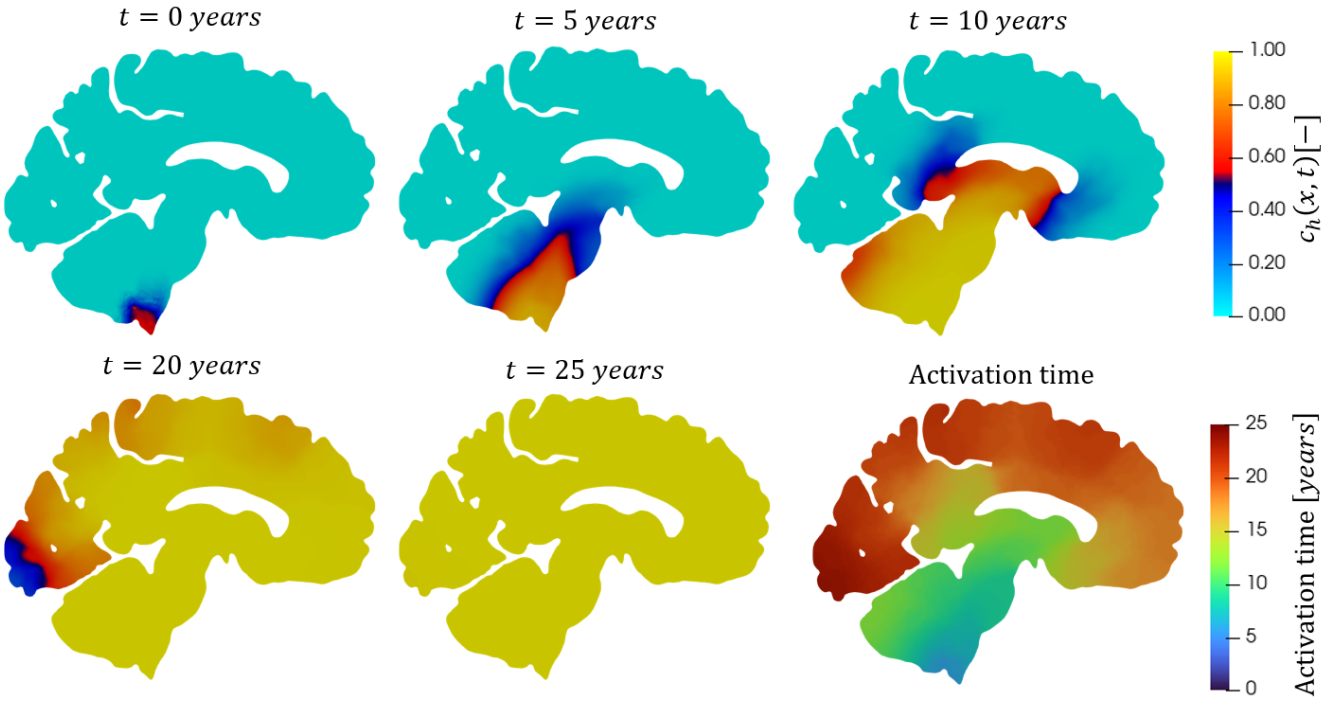

Figure 8 Test Case 5: computed α-synuclein concentration c_h across different years of pathology development using the FK model with polynomial order $p = 4$.

8.3 Test Case 5: Comparison with the FK model

We repeat the previous test case using the fully discrete FK formulation introduced in [13]. Keeping the same mesh and parameter setup, we simulate the spreading of α-synuclein in a 2D brain section. Figure 8 presents the solution at different time instants, showing strong agreement with the SFK results from Figure 7.To further evaluate the model, we compare the activation times computed by the two formulations. The resulting activation profiles are virtually identical, confirming the consistency between the FK and SFK approaches. Moreover, increasing the polynomial order and refining the mesh effectively suppresses numerical oscillations, confirming that both models converge toward the same propagation pattern under discretization refinement.To assess the robustness of the SFK model under lower-order discretizations, we repeat the simulation using $p = 1$ for both formulations. As shown in Figure 9, the SFK model accurately captures the expected propagation dynamics. In contrast, the FK model suffers from numerical instability, producing nonphysical negative values near the outer brain boundary that ultimately trigger divergence. This comparison underscores the ability of the SFK formulation to deliver reliable solutions even at low polynomial orders, significantly reducing computational overhead.

8.4 Test Case 6: Spreading of α-synuclein with grey-white matter distinction

In this test case, we simulate the spreading of α-synuclein protein in a 2D brain section taking into account the distinction between grey and white matter. We highlight the difference because grey matter can be approximately assumed isotropic, while white matter is mainly made of axons, whose fibres represent the principal direction of propagation of the electric signal. We select a unique extracellular diffusion magnitude $d_{ext} = 8$ mm^2/year, an axonal diffusion magnitude $d_{axn} = 0$ mm^2/year and a reaction parameter $\alpha = 0.45$/year for grey matter regions, and $d_{axn} = 80$ mm^2/year and $\alpha = 0.9$/year for white matter regions. The solution is computed using a timestep $\Delta t = 10^{-2}$ years on the agglomerated mesh introduced in Test Case 3. Moreover, we choose $\eta_0 = 10$, $f = 0$, and we assume homogeneous Neumann boundary conditions on $\partial\Omega$. As an initial condition, we consider a Gaussian distribution of proteins located in the

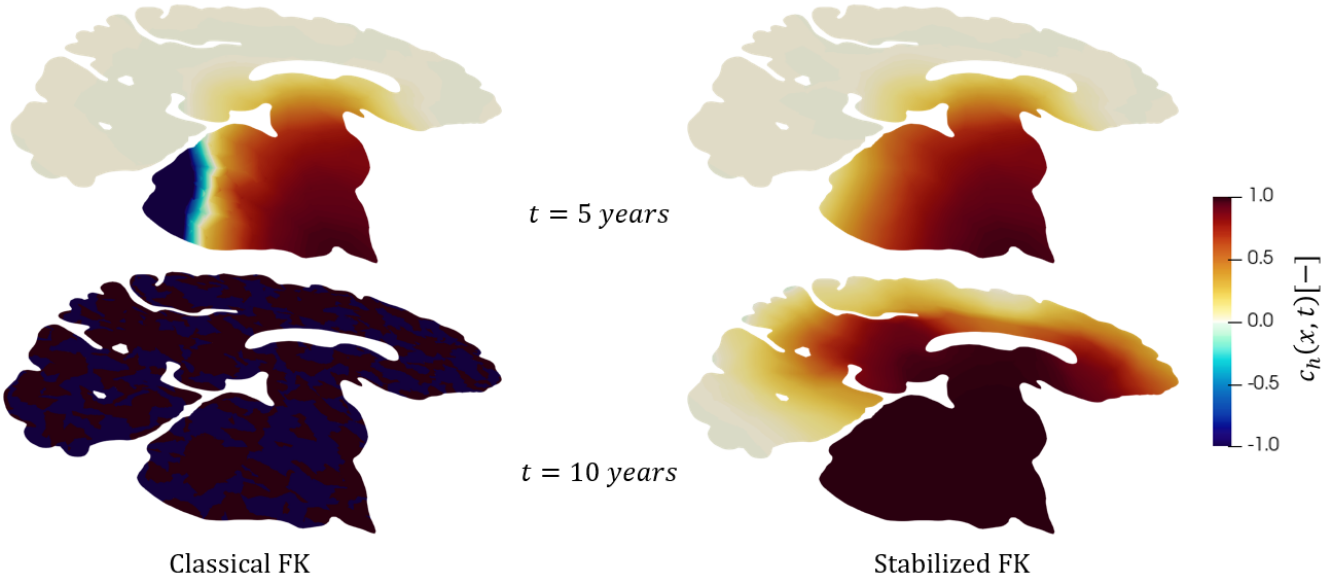

Figure 9 Test Case 5: comparison of computed α-synuclein concentration across different years of pathology development for the FK and SFK models with $p = 1$.

dorsal motor nucleus [20].

Figure 10 displays the computed solution at different time instants ($t = 10$ and $T = 25$ years) alongside the resulting activation times for both formulations. We observe that the progression of the disease remains coherent with the medical literature [20]. The activation time of the pathology is computed using (31); as expected from the concentration patterns, the activation of the pathology is not complete within the considered time frame. Moreover, the SFK model achieves the same accuracy and captures identical patterns as the FK model while employing a lower polynomial order ($p = 3$ for SFK versus $p = 4$ for FK). This reduction in the discretization order significantly lowers the computational cost, making the SFK formulation more efficient.

9 Conclusions

In this work, we proposed a polytopal discontinuous Galerkin discretization of a stabilized Fisher–Kolmogorov model obtained by introducing an absolute-value stabilization in the nonlinear reaction term. The resulting model and numerical scheme exhibit several key advantages. On the one hand, for non-negative continuous solutions, the formulation is strongly consistent with the original model, which is particularly relevant for biological applications. On the other hand, it ensures significantly improved stability properties. In addition, we derived stability and convergence error estimates for the proposed method on a general class of polytopal meshes. We provided numerical validation of the theoretical results in both two and three dimensions. We also simulated the diffusion of α-synuclein in a realistic 2D brain section, validating the outcomes by comparing activation times in selected brain regions with findings reported in the medical literature. Furthermore, a comparison with the non-stabilized formulation shows that the proposed method delivers reliable results even at low polynomial degrees, while maintaining high-order accuracy and computational efficiency.

Possible future developments include validation on realistic 3D brain geometries, enabling applications to patient-specific reconstructions. Another promising direction is the development of a space–time DG formulation [34, 35] to achieve higher-order convergence in time. Finally, the approach could be extended to other biological population dynamics models affected by similar instabilities near equilibrium states, which often compromise the robustness of standard numerical solvers.

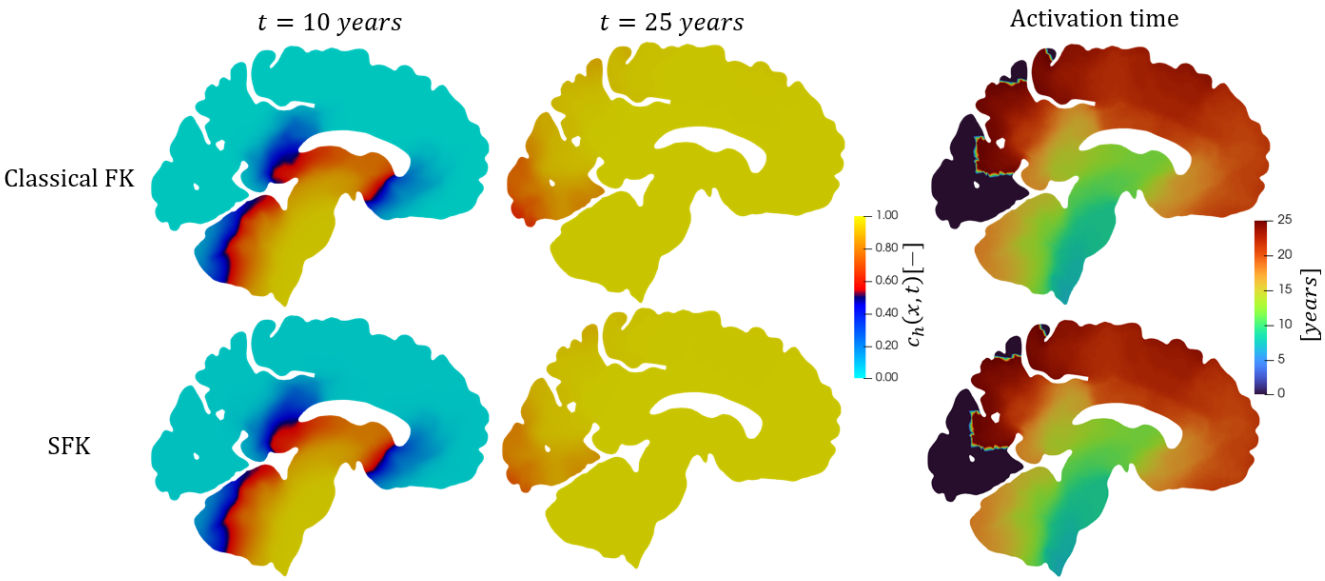

Figure 10 Test Case 6: patterns of computed α-synuclein concentration at $t = 10$ and $T = 25$ years, and corresponding pathology activation times, distinguishing between grey and white matter. Results are obtained using the FK model ($p = 4$) and the SFK model ($p = 3$).

Acknowledgements

OASIS-3 provided the brain MRI images: Longitudinal Multimodal Neuroimaging: Principal Investigators: T. Benzinger, D. Marcus, J. Morris; NIH P30 AG066444, P50 AG00561, P30 NS09857781, P01 AG026276, P01 AG003991, R01 AG043434, UL1 TR000448, R01 EB009352. AV-45 doses were provided by Avid Radiopharmaceuticals, a wholly-owned subsidiary of Eli Lilly.

References

[1] L. C. Walker and M. Jucker, "Neurodegenerative diseases: Expanding the prion concept," *Annual Review of Neuroscience*, vol. 38, no. 1, pp. 87–103, 2015.

[2] P. Calabresi, A. Mechelli, G. Natale, L. Volpicelli-Daley, G. Di Lazzaro, and V. Ghiglieri, "Alpha-synuclein in Parkinson's disease and other synucleinopathies: from overt neurodegeneration back to early synaptic dysfunction," *Cell Death & Disease*, vol. 14, no. 3, p. 176, 2023.

[3] G.-F. Chen, T.-H. Xu, Y. Yan, Y. Zhou, Y. Jiang, K. Melcher, and H. E. Xu, "Amyloid beta: structure, biology and structure-based therapeutic development," *Acta Pharmacologica Sinica*, vol. 38, no. 9, pp. 1205–1235, 2017.

[4] M. Jouanne, S. Rault, and A. Voisin-Chiret, "Tau protein aggregation in Alzheimer's disease: An attractive target for the development of novel therapeutic agents," *European Journal of Medicinal Chemistry*, vol. 139, pp. 153–167, 2017.

[5] B. Franchi and S. Lorenzani, "From a microscopic to a macroscopic model for Alzheimer disease: Two-scale homogenization of the Smoluchowski equation in perforated domains," *Journal of Nonlinear Science*, vol. 26, pp. 717–753, 2016.

[6] M. Bertsch, B. Franchi, N. Marcello, M. Tesi, and A. Tosin, "Alzheimer's disease: a mathematical model for onset and progression," *Mathematical Medicine and Biology: a Journal of the IMA*, vol. 34, no. 2, pp. 193–214, 2017.

[7] J. Weickenmeier, M. Jucker, A. Goriely, and E. Kuhl, "A physics-based model explains the prion–like features of neurodegeneration in Alzheimer's disease, Parkinson's disease, and amyotrophic lateral sclerosis," *Journal of the Mechanics and Physics of Solids*, vol. 124, pp. 264–281, 2019.

[8] S. Fornari, A. Schäfer, M. Jucker, A. Goriely, and E. Kuhl, "Prion-like spreading of Alzheimer's disease within the brain's connectome," *Journal of The Royal Society Interface*, vol. 16, no. 159, p. 20190356, 2019.

[9] C. Engwer and M. Wenske, "Estimating the extent of glioblastoma invasion," *Journal of Mathematical Biology*, vol. 82, no. 1, p. 10, 2021.

[10] J. Roessler and H. Hüssner, "Numerical solution of the 1 + 2 dimensional Fisher's equation by finite elements and the Galerkin method," *Mathematical and Computer Modelling*, vol. 25, no. 3, pp. 57–67, 1997.

[11] J. E. Macías-Díaz and A. Puri, "An explicit positivity-preserving finite-difference scheme for the classical Fisher–Kolmogorov–Petrovsky–Piscounov equation," *Applied Mathematics and Computation*, vol. 218, no. 9, pp. 5829–5837, 2012.

[12] T. Gortsas, S. Tsinopoulos, and D. Polyzos, "A local domain boundary element method for solving the nonlinear Fisher KPP diffusion-reaction equation," *Engineering Analysis with Boundary Elements*, vol. 138, pp. 177–188, 2022.

[13] M. Corti, F. Bonizzoni, L. Dede', A. M. Quarteroni, and P. F. Antonietti, "Discontinuous Galerkin methods for Fisher-Kolmogorov equation with application to α-synuclein spreading in Parkinson's disease," *Computer Methods in Applied Mechanics and Engineering*, vol. 417, p. 116450, 2023.

[14] M. Corti, F. Bonizzoni, and P. F. Antonietti, "Structure preserving polytopal discontinuous Galerkin methods for the numerical modeling of neurodegenerative diseases," *Journal of Scientific Computing*, vol. 100, p. 39, 2024.

[15] P. F. Antonietti, M. Corti, S. Gómez, and I. Perugia, "A structure-preserving LDG discretization of the Fisher–Kolmogorov equation for modeling neurodegenerative diseases," *Mathematics and Computers in Simulation*, vol. 241, pp. 351–366, 2026.

[16] S. Salsa and G. Verzini, *Partial differential equations in action. From modelling to theory.* Cham: Springer, 2022.

[17] A. Cangiani, E. H. Georgoulis, and P. Houston, "hp-version discontinuous Galerkin methods on polygonal and polyhedral meshes," *Mathematical Models and Methods in Applied Sciences*, vol. 24, no. 10, pp. 2009–2041, 2014.

[18] A. Cangiani, Z. Dong, E. H. Georgoulis, and P. Houston, *hp-version discontinuous Galerkin methods on polygonal and polyhedral meshes.* Springer, 2017.

[19] P. F. Antonietti, M. Corti, and G. Martinelli, "Polytopal mesh agglomeration via geometrical deep learning for three-dimensional heterogeneous domains," *Mathematics and Computers in Simulation*, vol. 241, pp. 335–353, 2026.

[20] H. Braak, K. Tredici, U. Rüb, R. de Vos, E. Jansen Steur, and E. Braak, "Staging of brain pathology related to sporadic Parkinson's disease," *Neurobiology of Aging*, vol. 24, no. 2, pp. 197–211, 2003.

[21] M. Goedert, "Alzheimer's and Parkinson's diseases: The prion concept in relation to assembled Aβ, tau, and α-synuclein," *Science*, vol. 349, p. 6248, 2015.

[22] D. Di Pietro and J. Droniou, *The Hybrid High-Order Method for Polytopal Meshes: Design, Analysis and Applications*. Cham:Springer, 2020.

[23] D. N. Arnold, F. Brezzi, B. Cockburn, and L. D. Marini, "Unified analysis of discontinuous Galerkin methods for elliptic problems," *SIAM Journal on Numerical Analysis*, vol. 39, no. 5, pp. 1749–1779, 2001-02.

[24] I. Babuška and M. Suri, "The p and $h-p$ versions of the finite element method, basic principles and properties," *SIAM review*, vol. 36, no. 4, pp. 578–632, 1994.

[25] A. Cangiani, Z. Dong, and E. Georgoulis, "hp-version discontinuous galerkin methods on essentially arbitrarily-shaped elements," *Mathematics of Computation*, vol. 91, no. 333, pp. 1–35, 2022.

[26] M. Botti and L. Mascotto, "Sobolev-Poincaré inequalities for piecewise $W^{1,p}$ functions over general polytopic meshes," *SIAM Journal on Numerical Analysis*, vol. In press, 2026.

[27] A. Quarteroni, *Numerical models for differential problems*. Cham: Springer, 3 ed., 2017.

[28] P. Antonietti, S. Bonetti, M. Botti, M. Corti, I. Fumagalli, and I. Mazzieri, "`lymph`: Discontinuous Polytopal Methods for Multi-Physics Differential Problems," *ACM Transactions on Mathematical Software*, vol. 51, no. 1, 2025.

[29] C. Talischi, G. Paulino, P. Anderson, and I. Menezes, "`PolyMesher`: A general-purpose mesh generator for polygonal elements written in Matlab," *Structural and Multidisciplinary Optimization*, vol. 45, no. 3, pp. 309–328, 2012.

[30] P. Antonietti, M. Caldana, F. Daniele, N. D. March, I. Fumagalli, I. Mazzieri, S. Pagani, P. Peixoto, and F. Rosnati, "Vulpes: a flexible and parallel computational library for high-order discontinuous polytopal element simulations." 2026, in preparation (https://vulpeslib.github.io/).

[31] C. H. Rycroft, "Voro++: A three-dimensional voronoi cell library in c++," *Chaos*, vol. 19, p. 041111, dec 2009.

[32] P. F. Antonietti, F. Bonizzoni, M. Corti, and A. Dall'Olio, "Discontinuous Galerkin approximations of the heterodimer model for protein-protein interaction," *Computer Methods in Applied Mechanics and Engineering*, vol. 431, p. 117282, 2024.

[33] A. Schäfer, J. Weickenmeier, and E. Kuhl, "The interplay of biochemical and biomechanical degeneration in Alzheimer's disease," *Computer Methods in Applied Mechanics and Engineering*, vol. 352, pp. 369–388, 2019.

[34] P. Antonietti, I. Mazzieri, and F. Migliorini, "A space-time discontinuous Galerkin method for the elastic wave equation," *Journal of Computational Physics*, vol. 419, p. 109685, 2020.

[35] P. Antonietti, I. Mazzieri, and F. Migliorini, "A discontinuous Galerkin time integration scheme for second order differential equations with applications to seismic wave propagation problems," *Computers & Mathematics with Applications*, vol. 134, pp. 87–100, 2023.

MOX Technical Reports, last issues

Dipartimento di Matematica
Politecnico di Milano, Via Bonardi 9 - 20133 Milano (Italy)

65/2026 De Sanctis, M.F.; Arnone, E.; Ieva, F.; Sangalli, L.M.
Modeling group heterogeneity in spatio-temporal data via physics-informed regression

64/2026 Radisic, I.; Tirotta, R.; Zingaro, A.; Pagani, S.; Dede', L.
Physics-Informed Neural Networks for the High-Resolution Reconstruction of Flow Measurement Indicators in Fluid Dynamics

62/2026 Ciaramella, G.; Gong, W.; Kwok, F.; Tan, Z.
On the Uniform Convergence Analysis of the Schwarz Alternating Method for Optimal Control Problems

63/2026 Ciaramella, G.; Gong, W.; Kwok, F., Tan, Z.
Uniform Convergence of the Schwarz Alternating Method for Optimal Control Problems

60/2026 Ciaramella, G.; Gander, M.J.; Van Criekingen, S.; Vanzan, T.
Algebraic and Two-Level Parallel Substructured Schwarz Methods

58/2026 Mapelli, A.; Massi, M.C.; Cuccuru, G.; Di Angelantonio, E.; Ieva, F.
Prior-informed conditional Gaussian graphical models: an application to protein interaction network reconstruction

57/2026 Fontana, N.; Secchi, P.; Di Angelantonio, E.; Ieva, F.
Modeling time-varying genetic effects on binary disease risk via functional Mendelian Randomization

56/2026 Botta, P.; Vitullo, P.; Ventimiglia, T.; Linninger, A.; Zunino, P.
Physics-Informed Learning of Microvascular Flow Models using Graph Neural Networks

55/2026 Beirao da Veiga, L.; Canuto, C.; Nochetto, R.H.; Vacc, G ; Verani, M.
A Virtual Element Method for elliptic problems on trimmed background meshes

51/2026 Bellezza P.; Ciaramella G.; Macchini C.; Mazzieri I.; Verani M.
ParaFlow: Parareal Acceleration of Gradient-Flow Minimization